# Vanadium-incorporated CoP2 with lattice expansion for highly efficient acidic overall water splitting

**Yu Wang**
Heilongjiang University
**Yanqing Jiao**
Key Laboratory of Functional Inorganic Material Chemistry, Ministry of Education of the People's Republic of China
**Ganceng Yang**
Heilongjiang University
**Haijing Yan**
Heilongjiang University
**Chungui Tian**
Key Laboratory of Functional Inorganic Material Chemistry, Ministry of Education of the People's Republic of China
**Aiping Wu**
Key Laboratory of Functional Inorganic Material Chemistry, Ministry of Education of the People's Republic of China
**Yue Liu**
Heilongjiang University
**Honggang Fu** ( fuhg@vip.sina.com )
Heilongjiang University

**Article**

**Keywords:** proton exchange membrane water electrolyzer, noble-metal catalysts, V-CoP2 porous nanowires

**Posted Date:** September 15th, 2021

**DOI:** https://doi.org/10.21203/rs.3.rs-898273/v1

# Vanadium-incorporated $CoP_2$ with lattice expansion for highly efficient acidic overall water splitting

Yu Wang, Yanqing Jiao, Ganceng Yang, Haijing Yan,* Chungui Tian, Aiping Wu, Yue Liu, and Honggang Fu*

**Abstract:** Proton exchange membrane water electrolyzer (PEMWE) in acidic media is a hopeful scenario for hydrogen production by using renewable energy sources, but the grand challenge lies in substituting active and stable noble-metal catalysts. Herein, a robust electrocatalyst of V-$CoP_2$ porous nanowires arranged on carbon cloth is successfully fabricated *via* incorporating vanadium into $CoP_2$ lattice. Structural characterizations and theoretical analysis indicate that lattice expansion of $CoP_2$ caused by V incorporation results in the upshift of d-band center, which is conducive to hydrogen adsorption for boosting HER activity. Besides, V promotes surface reconstruction to generate a thicker $Co_3O_4$ layer that enhances acid-corrosion resistance and optimizes the adsorption of water and oxygen-containing species, thus improving OER activity and stability. Accordingly, it presents a superior acidic overall water splitting activity (1.47 V@10 mA $cm^{-2}$) over Pt-C/CC||$RuO_2$/CC, and remarkable stability. This work proposes a new route to design efficient electrocatalysts *via* lattice engineering for PEMWE.

Key Laboratory of Functional Inorganic Material Chemistry Ministry of Education of the People's Republic of China Heilongjiang University, Harbin 150080.
email: fuhg@vip.sina.com, fuhg@hlju.edu.cn, yanhaijing@hlju.edu.cn.

Replacing the fossil fuels is of great significance for sustainable energy supply[1,2]. Among the various alternatives, hydrogen produced by water electrolysis and renewable energy sources (solar, wind etc.) has been considered as one of the most promising solutions[3,4]. More attentions focus on the conventional alkaline water electrolyzer (AWE), in view of its permission to employ the cost-effective electrocatalysts for cathodic hydrogen evolution reaction (HER) and anodic oxygen evolution reaction (OER)[5,6]. However, due to narrow load range and poor flexibility, it can be only driven by stable thermal power generation[7,8]. Recently, proton exchange membrane water electrolyzer (PEMWE) with easy assembly with renewable energy sources is highlighted as the new-generation candidate, in view of great power density, high efficiency at low temperature and low gas crossover[9,10]. Generally, noble-metal-based materials (Pt and Ir, Ru oxides) are the benchmark HER and OER electrocatalysts in acidic media with high activity and durability, but suffer from high cost and scarcity[11-13]. To this end, earth-abundant transition metal-based materials (e.g. phosphides, chalcogenides, nitrides, carbides etc.) have been developed to accelerate HER and OER[14,15]. Despite gratifying advances have been made in the past decades, the HER performance is still far from Pt in acidic condition[16,17]. Especially in acidic OER process, most of them are unstable in high oxidation potential according to Pourbaix diagrams[18]. Therefore, developing cost-effective and durable HER/OER electrocatalysts in acidic media is crucial but challenging for the large-scale application of PEMWE.

Transition metal phosphides, particularly cobalt-based phosphides, have been investigated as promising noble-metal alternatives for HER and OER owing to the high electrical conductivity and noble-metal like properties[19-22]. For instance, Co-phosphides with various stoichiometric ratios show efficient HER activity in acidic, neutral and alkaline solutions[23]. Geyer et al. reported that the catalytic HER activity of cobalt-based phosphides increased with the elevating phosphorous content ($CoP_2$ > CoP > $Co_2P$)[19]. Recently, Co-phosphides also act as OER electrocatalysts in alkaline medium with the characteristic of surface reconstruction to form the corresponding oxides/hydroxides[24]. For example, Xing et al. confirmed CoP nanorods

could catalyze OER in 1 M KOH up to 12h, and further verified the good stability was benefited from the generated ultrafine crystalline $Co_2O_3$ layer on the CoP surface[25]. It is shown that Co-oxides can not only stabilize in alkaline media, but also own adequate acid-resistance capacity that can perform a lengthy operation in acidic solution under high anodic potential[26]. Enlightened by above, utilizing the surface reconstruction of cobalt phosphides, the acid-stable OER catalysts may be achieved. To resist strong acid corrosion, the reconstructed oxide layer should be fulfilled to a certain thickness. Although surface reconstruction of pure Co-phosphides will happen naturally during OER electrolysis, the thin surface reconstruction is not enough to resist strong acid corrosion[27,28]. We consider whether any tactics could be adopted to manipulate the surface reconstruction of Co-phosphides and simultaneously increase the thickness of reconstruction layer, thus further improving the OER stability.

Heteroatom incorporation has emerged as one of the most effective approaches to improve the intrinsic activities for HER and OER[29,30]. Because heteroatom incorporation can change the crystal environment of host material and regulate the electronic structure, which strengthes the adsorption behaviors of reactive intermediates, thus greatly promoting catalytic activity[31]. Vanadium (V) is an ideal dopant in terms of its abundant resources, variable valence, acid corrosion resistance and adaptive atomic radius close to cobalt[32]. Wang et al. reported V-doped $Co_4N$ with prominent HER catalytic activity due to that V doping tailors the d-band center[33]. Hu et al. designed V "bridge" between Co-O bonds in $CoV_2O_6$ nanowires, which enhances the conductivity, resulting in boosted OER activity in alkaline media[34]. Hence, we expect that the HER activity of Co-phosphides can be improved through adjusting electronic structure after vanadium incorporation. Meanwhile, utilizing the positive role of V on Co-phosphides controls surface reconstruction, thus improving the OER stability in acidic media. To our knowledge, studies on this aspect have never been reported.

Herein, we fabricated vanadium incorporated cobalt diphosphide porous nanowires on carbon cloth (denoted as V-$CoP_2$/CC) by a facile two-step method involving hydrothermal treatment and subsequent phosphorization. The lattice

expansion of $CoP_2$ caused by V incorporation decreases the overlap of atomic wave functions, leading to upshift of d-band center, which conduces to hydrogen adsorption on P sites for promoting HER. Besides, V promotes surface construction to generate a thicker $Co_3O_4$ layer on the surface of $CoP_2$ that enhances acid-corrosion resistance and optimizes the adsorption free energies of water and oxygen-containing species, which is responsible for OER activity and stability. Accordingly, it presents low overpotentials of 50 and 91 mV at 10 mA $cm^{-2}$ for HER and OER in acidic media, as well as remarkable stability. Furthermore, the assembled overall water splitting cell by employing V-$CoP_2$/CC as both electrodes shows a superior acidic overall water splitting activity (1.47 V@10 mA $cm^{-2}$) than Pt-C/CC||$RuO_2$/CC, and remarkable stability. Additionally, it can be powered by a solar cell to continuously produce the hydrogen and oxygen gases, implying its great potential for coupling with renewable energy sources.

## Results and discussion

**Catalyst synthesis and characterization.** As depicted in Fig. 1a, V-$CoP_2$/CC sample was prepared through hydrothermal synthesis of V-incorporated CoOOH on the carbon cloth (V-CoOOH/CC) and followed by phosphatizing treatment. Briefly, V-CoOOH nanowire arrays were evenly grown on the surface of carbon cloth by hydrothermal method at 120 $^oC$ for 4h (Supplementary Fig. 1, Fig. 2). Afterwards, the as-prepared V-CoOOH nanowires were phosphatized at 600 $^oC$ for 2h, generating V-$CoP_2$ porous nanowires with the V incorporation ratio of 5%. For comparison, pure-phase $CoP_2$ grown on the carbon cloth (labeled as $CoP_2$/CC) was prepared through a similar route without adding V source. Scanning electron microscopy (SEM) and transition electron microscopy (TEM) images of $CoP_2$/CC show $CoP_2$ nanowires with the width of ~100 nm arranged on CC are smooth and solid (Fig. 1b-c and Supplementary Fig. 3). After introducing V, the nanowires arranged on CC remain intact, but become coarse with many pores appeared (Fig. 1d-e). Pore information is further verified by $N_2$ adsorption-desorption measurement (Fig. 1f). V-$CoP_2$/CC delivers higher specific surface area (22.8 $m^2$ $g^{-1}$) with average pore diameter of ~14

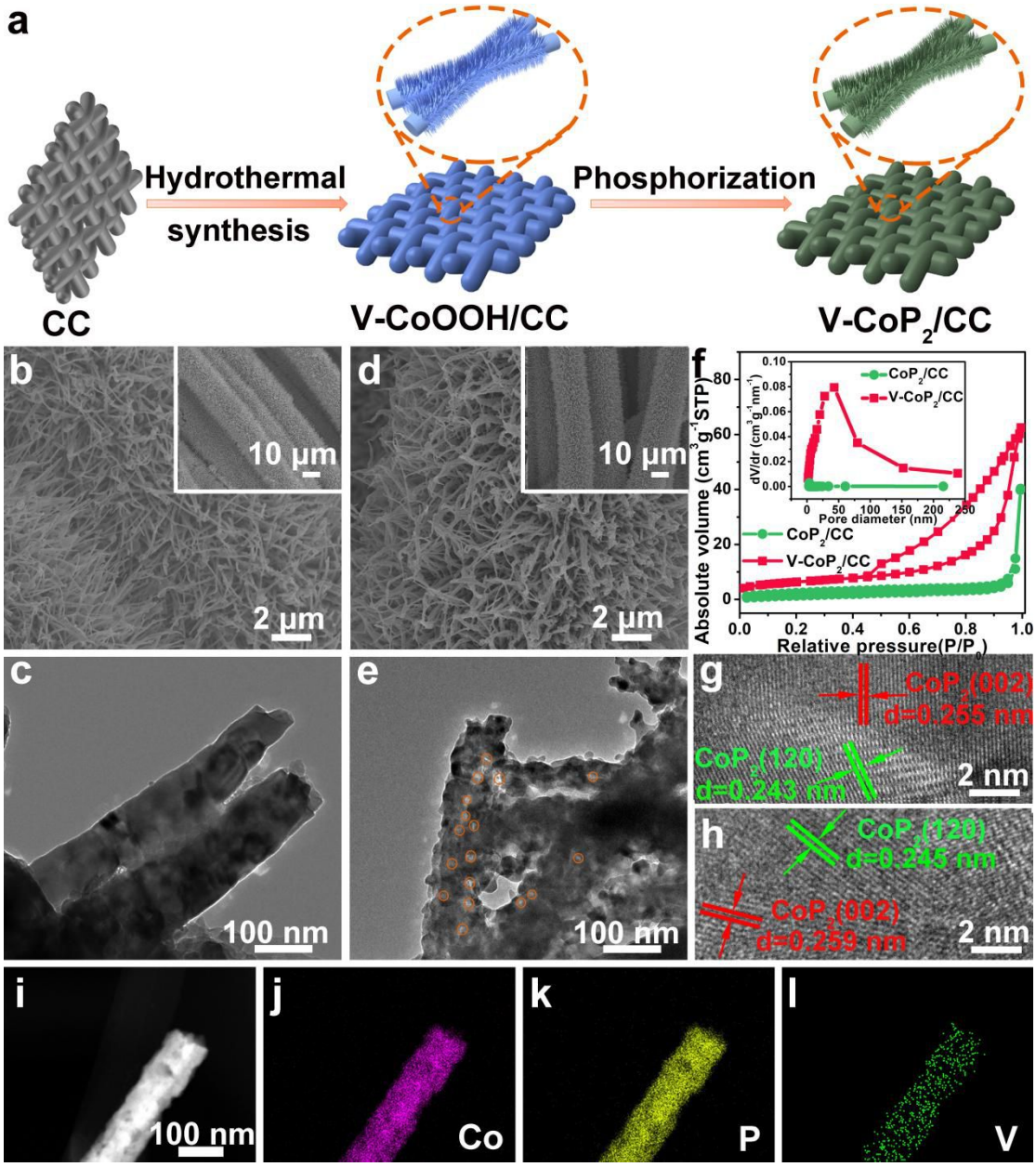


**Fig. 1 Material synthesis and morphological characterization.** (a) Schematic diagram of the synthesis of V-$CoP_2$/CC. (b, c) SEM and TEM images of $CoP_2$/CC. (d, e) SEM and TEM images of V-$CoP_2$/CC. (f) $N_2$ adsorption-desorption isotherms (Inset: pore size distribution). (g, h) HRTEM images of $CoP_2$/CC and V-$CoP_2$/CC. (i) STEM image and the corresponding EDX elemental mappings of (j) Co, (k) P and (l) V of V-$CoP_2$.

nm relative to nonporous $CoP_2$/CC (5.4 $m^2$ $g^{-1}$), which is in consistent with TEM observations. Such porous nanowire structure can undoubtedly increase active surface area, promote rapid transport of electrons/reactants, and accelerate the release of gas, thus greatly boosting the electrocatalytic performance. Additionally, the influence of V incorporation ratio, and other synthetic conditions (hydrothermal and phosphorization parameters) on the morphology and structure of V-$CoP_2$/CC was also

studied (Supplementary Table 1 and Fig. 4-Fig. 7). As shown, appropriate synthetic condition is important to produce V-$CoP_2$/CC with well-confined porous nanowire structure. High-resolution TEM (HRTEM) image of $CoP_2$/CC exhibits clear lattice fringes with interplanar distances of 0.243 and 0.255 nm, which can be indexed to the (120) and (002) planes of $CoP_2$ (Fig. 1g). In contrast, for V-$CoP_2$, the interplanar distances of (120) and (002) facets increase, proving that V incorporation causes lattice expansion (Fig. 1h). STEM image and the corresponding EDX element mappings manifest the uniform distribution of Co, P and V elements in V-$CoP_2$ (Fig. 1i-l), further illustrating the successful incorporation of V into $CoP_2$.

The change of $CoP_2$ by V incorporation is further investigated by a series of characterizations. The crystal models of $CoP_2$ and V-$CoP_2$ are firstly established to determine the influence of V incorporation on the electronic structure of $CoP_2$. Fig. 2a displays the crystal structure of $CoP_2$ and V-$CoP_2$. As depicted, the lattice constants increase obviously after V incorporation, which indicates the emergence of lattice expansion, in good agreement with HRTEM observations. X-ray diffraction (XRD) pattern of $CoP_2$/CC exhibits a diffraction peak at 26.5° assigned to the (002) facet of graphite from carbon cloth, and other diffraction peaks indexed to $CoP_2$ (PDF No. 77-0263) (Fig. 2b). The XRD pattern of V-$CoP_2$ displays quite similar to that of $CoP_2$, but the diffraction peaks slightly move to the lower angle region, illustrating that V incorporation causes a certain expansion of interplanar distance without changing the intrinsic structure of $CoP_2$[35,36]. Raman spectra of V-$CoP_2$ and $CoP_2$ in Fig. 2c reveals that the incorporation of V into $CoP_2$ results in a slight blue-shift of the characteristic peaks, further confirming lattice expansion of $CoP_2$ due to V incorporation[37]. To further verify the existence of V and investigate the effect of V on electron structure of $CoP_2$, X-ray photoelectron spectroscopy (XPS) spectra of $CoP_2$ and V-$CoP_2$ were carried out. Survey spectra (Supplementary Fig. 8) show the presence of Co, P and O elements both in $CoP_2$/CC and V-$CoP_2$/CC, apart from the emergence of V element in V-$CoP_2$/CC. The O comes from the superficial oxidation of phosphides exposed in air[38]. As shown in Fig. 2d, Co XPS spectrum of V-$CoP_2$/CC presents three doublet peaks corresponding to Co-P bond (782.1/798.5 eV), Co-O bond (784.2/802.9 eV)

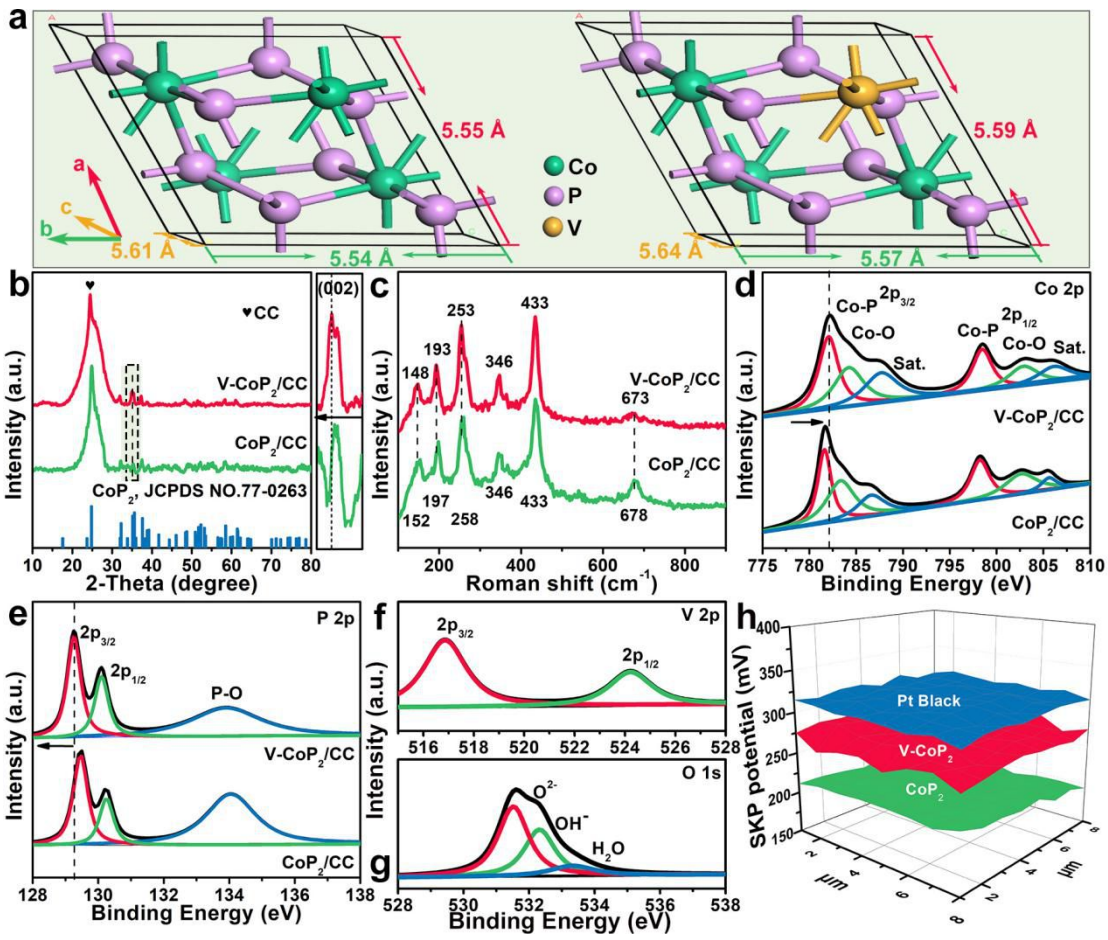


**Fig. 2 Structural characterization.** (a) Crystal models of $CoP_2$ and V-$CoP_2$ with lattice constants. (b) XRD pattern and (c) Raman spectra of $CoP_2$/CC and V-$CoP_2$/CC. XPS spectra of (d) Co 2p and (e) P 2p for $CoP_2$/CC and V-$CoP_2$/CC. XPS spectra of (f) V 2p and (g) O 1s for V-$CoP_2$/CC. (h) WF drawings of $CoP_2$, V-$CoP_2$ and Pt black.

from the superficial oxidation, and satellite signals (787.7/806.2 eV) of Co $2p_{3/2}$ and Co $2p_{1/2}$, respectively[39]. As for P 2p XPS spectrum (Fig. 2e), two peaks located at 129.5 and 130.3 eV are assigned to the Co-P bond of P $2p_{3/2}$ and P $2p_{1/2}$[40]. The peak located at 134.1 eV is attributed to P-O bond from superficial oxidation[40]. The V 2p spectrum of V-$CoP_2$/CC is detected (Fig. 2f), with two predominant peaks located at 516.9 and 524.2 eV corresponding to V $2p_{3/2}$ and V $2p_{1/2}$, which is the characteristic of $V^{4+}$ [41]. The ionic radius of V in the valence of 4 is 0.58 Å, slightly large than that of Co (0.55 Å)[42]. In this case, $V^{4+}$ ion can easily insert into the lattice of $CoP_2$, thus causing lattice expansion. The O 2p region can be deconvoluted three peaks, being indexed to oxygen from metal-O, hydroxides and adsorbed $H_2O$ (Fig. 2g)[43]. Above results further confirm the successful incorporation of V in $CoP_2$. Notably, the peak positions of Co element in V-$CoP_2$ shift towards higher binding energy (0.5 eV) in

comparison with that of $CoP_2$, illustrating that the chemical environment of Co ion is modified by incorporating V species. Meanwhile, the binding energy of P reduces 0.4 eV after V incorporation, indicating the increased electron density around P sites in V-$CoP_2$[44]. These results manifest the electron structure modulation effect by incorporating V, which is significant in regulating catalytic activity[45,46]. Additionally, the work function (WF) values, calculated by performing the scanning Kelvin probe (SKP) measurement, for $CoP_2$, V-$CoP_2$ and Pt black are 5.55, 5.61 and 5.65 eV, respectively (Fig. 2h). Compared to $CoP_2$, the WF of V-$CoP_2$ is higher and much closer to that of Pt, signifying V incorporation induces electronic characteristic more similar to Pt, which is undoubtedly favorable for electrocatalysis.

**Electrocatalytic hydrogen evolution.** The HER performance of the as-prepared V-$CoP_2$/CC electrode was evaluated in acidic solution using a typical three-electrode system. Bare CC, $CoP_2$/CC, and Pt-C coated on CC (Pt-C/CC) were tested for comparison. The iR-compensated linear sweep voltammetry (LSV) curves show that V-$CoP_2$/CC presents the excellent catalytic activity. Specifically, V-$CoP_2$/CC requires an onsetpotential ($\eta_{onset}$) of zero, which is comparable to that of Pt-C/CC (Fig. 3a). V-$CoP_2$/CC also shows overpotential advantage at large current densities. The overpotentials to achieve the current densities of 10, 50 and 100 mA $cm^{-2}$ are 50 ($\eta_{10}$), 134 ($\eta_{50}$) and 181 mV ($\eta_{100}$) for V-$CoP_2$/CC, which much lower than those of $CoP_2$/CC (123, 257 and 355 mV), and approach those of Pt-C/CC (32, 71 and 107 mV) (Fig. 3b and Supplementary Table 2). Furthermore, the superiority of V-$CoP_2$/CC over the other reported Co-based and V-based electrocatalysts in acidic media is also confirmed (Supplementary Table 3).

To inspect the HER kinetics, Tafel plots were calculated by the LSV curves as depicted in Fig. 3c. The measured Tafel slope for V-$CoP_2$/CC is 32 mV $dec^{-1}$, which is much smaller than that of $CoP_2$/CC (89 mV $dec^{-1}$) and much close to that of Pt-C/CC (31 mV $dec^{-1}$), suggesting the Volmer-Tafel mechanism for V-$CoP_2$/CC. The electrochemical impedance spectroscopy (EIS) was performed to study the reaction kinetics. Apparently, V-$CoP_2$/CC delivers a smaller charge transfer resistance ($R_{ct}$) of ~2 Ω than $CoP_2$/CC (~7 Ω) (Fig. 3d), which implies the enhanced charge transfer

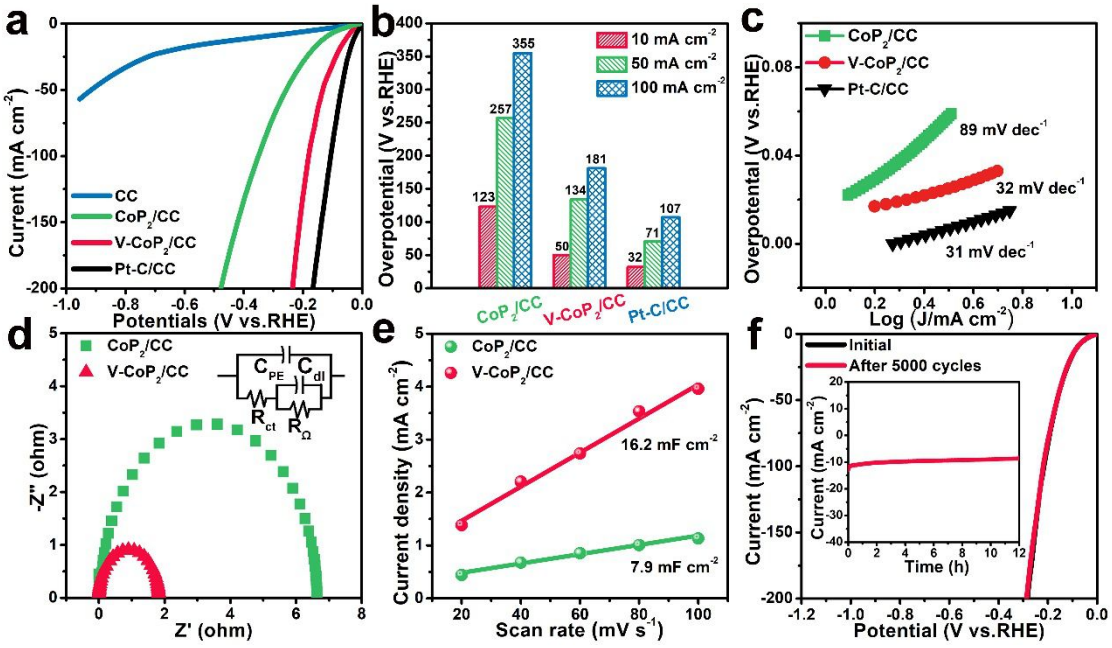


**Fig. 3 Electrochemical HER performance**. (a) LSV curves of CC, $CoP_2$/CC, V-$CoP_2$/CC and Pt-C/CC in 0.5 M $H_2SO_4$. (b) Comparison of overpotentials at 10, 50 and 100 mA $cm^{-2}$ and (c) Tafel plots for $CoP_2$/CC, V-$CoP_2$/CC and Pt-C/CC. (d) Nyquist plots and (e) capacitive currents at 0.1 V as a function of the scan rate for $CoP_2$/CC and V-$CoP_2$/CC. (f) LSV curves of V-$CoP_2$/CC before and after 5000 cycles. Insert: I-t chronoamperometric curve for V-$CoP_2$/CC during HER process for 12h.

kinetics contributed by vanadium incorporation. Additionally, the dependencies of the HER activity on the incorporation concentration, as well as hydrothermal and phosphorization conditions were also investigated. Clearly, V-$CoP_2$/CC obtained by V incorporation ratio of 5%, along with hydrothermal time of 2h and phosphrization at 600 $^oC$ for 2h exhibits the maximum HER activity (Supplementary Fig. 9-Fig. 12). Electrochemical active surface area (ECSA) was calculated through the double layer capacitance ($C_{dl}$) from the cyclic voltammetry (CV) method (Supplementary Fig. 13). V-$CoP_2$/CC possesses a larger $C_{dl}$ of 16.2 mF $cm^{-2}$ than $CoP_2$/CC (7.9 mF $cm^{-2}$). The high $C_{dl}$ of V-$CoP_2$/CC stands that appropriate vanadium incorporation brings in more active sites, benefiting to good HER performance (Fig. 3e). Furthermore, LSV curves normalized by ESCA were employed to estimate the specific catalytic activity. As depicted in Supplementary Fig. 14, V-$CoP_2$/CC still shows better HER performance. To further investigate the intrinsic catalytic activity, turnover frequency (TOF) and exchange current density ($j_0$) are evaluated. V-$CoP_2$/CC shows higher TOF value of 0.379 $s^{-1}$ at 100 mV than

$CoP_2$/CC (0.137 $s^{-1}$) (Supplementary Fig. 15). Meanwhile, the $j_0$ of V-$CoP_2$/CC (0.318 mA $cm^{-2}$) is consistently larger that of $CoP_2$/CC (0.207 mA $cm^{-2}$) (Supplementary Fig. 16). The large specific activity, TOF and $j_0$ values of V-$CoP_2$/CC demonstrate that vanadium incorporation induces the essential change on catalytic surface of $CoP_2$. Last, the stability of V-$CoP_2$/CC was assessed by CV cycles and I-t chronoamperometric tests. The polarization curve of V-$CoP_2$/CC presents a negligible catalytic degradation after 5000 CV cycles (Fig. 3f). The I-t chronoamperometric test of V-$CoP_2$/CC exhibits an ignorable loss of current density even after 12h (inset of Fig. 3f). Both of the tests validate its superb stability. The structural information of V-$CoP_2$/CC after HER electrocatalysis was further investigated. V-$CoP_2$/CC still maintains the nanowire morphology and show a negligible structure and composition change (Supplementary Fig. 17, Fig. 18), suggesting that there is no obvious surface reconstruction during HER electrolysis and the boosted HER activity mainly comes from the V incorporation.

**Electrocatalytic oxygen evolution.** The anodic OER performance was also evaluated. As shown in Fig. 4a, V-$CoP_2$/CC performs a low $\eta_{onset}$ of 70 mV, which is better than $RuO_2$/CC (185 mV). Moreover, V-$CoP_2$/CC presents the lowest overpotentials of 91, 320 and 498 mV at 10, 50 and 100 mA $cm^{-2}$, as compared with $CoP_2$/CC (246, 561 and 714 mV) and $RuO_2$/CC (235, 497 and 608 mV) (Fig. 4b and Supplementary Table 2). It also outperforms the recently reported noble-metal-based OER catalysts in acidic solution (Supplementary Table 4). In addition, V-$CoP_2$/CC exhibits a lowest Tafel slope of 40 mV $dec^{-1}$ relative to $CoP_2$/CC (117 mV $dec^{-1}$) and $RuO_2$/CC (82 mV $dec^{-1}$) (Fig. 4c), illustrating the optimum OER kinetics. V-$CoP_2$/CC delivers a smaller $R_{ct}$ of ~4 Ω than $CoP_2$/CC (~12 Ω), further suggesting the promoted OER kinetics by vanadium incorporation (Fig. 4d). Coincident with HER performance, V-$CoP_2$/CC with V incorporation ratio of 5%, prepared by hydrothermal time of 2h and phosphorization at 600 °C for 2h shows the best OER activity (Supplementary Fig. 19-Fig. 22). Besides, as determined by CV curves (Supplementary Fig. 23), V-$CoP_2$/CC possesses a larger $C_{dl}$ of 32.5 mF $cm^{-2}$ than $CoP_2$ (14.2 mF $cm^{-2}$), indicating more active sites caused by V incorporation (Fig. 4e). Accordingly,

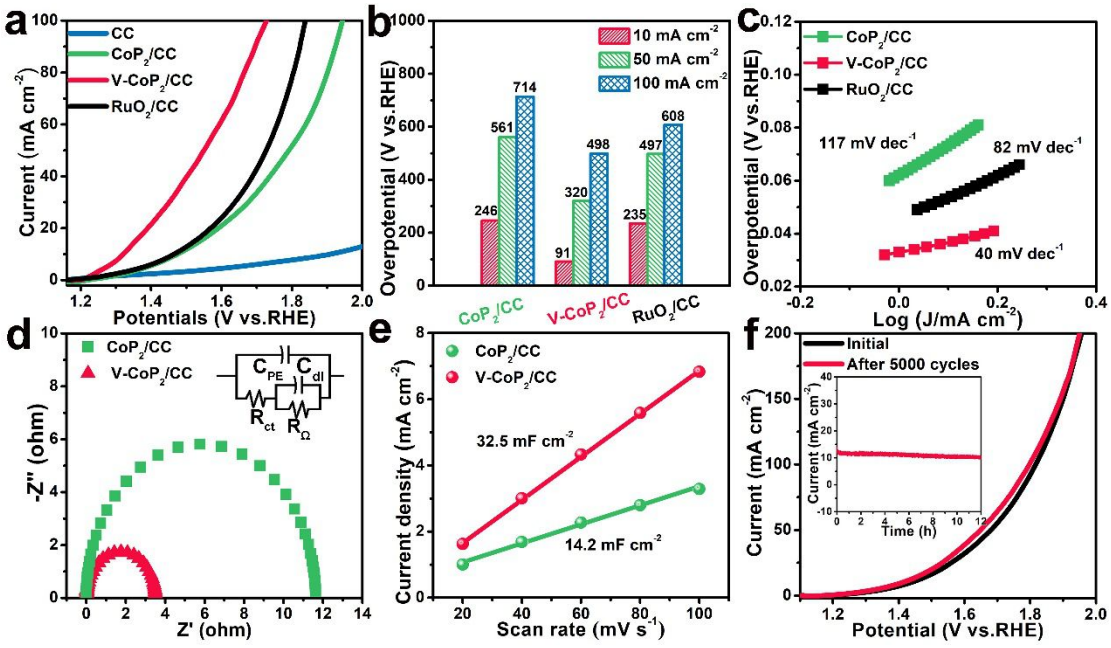


**Fig. 4 Electrochemical OER performance.** (a) LSV curves of CC, $CoP_2$/CC, V-$CoP_2$/CC and $RuO_2$/CC in 0.5 M $H_2SO_4$. (b) Comparison of overpotentials at 10, 50 and 100 mA $cm^{-2}$ and (c) Tafel plots for $CoP_2$/CC, V-$CoP_2$/CC and $RuO_2$/CC. (d) Nyquist plots and (e) capacitive currents at 1.15 V as a function of the scan rate for $CoP_2$/CC and V-$CoP_2$/CC. (f) LSV curves of V-$CoP_2$/CC before and after 5000 cycles. Insert: i-t chronoamperometric curve for V-$CoP_2$/CC during OER process for 12h.

the ESCA-normalized specific activity of V-$CoP_2$/CC surpasses that of $CoP_2$/CC (Supplementary Fig. 24). V-$CoP_2$/CC also exhibits a higher TOF value of 0.207 $s^{-1}$ at overpotential of 240 mV than $CoP_2$/CC (0.096 $s^{-1}$) (Supplementary Fig. S25). These results manifest the synchronously increased active sites and intrinsic activity by V incorporation. The V-$CoP_2$/CC catalyst shows no obvious loss of current density no mater after CV cycles or I-t chronoamperometric test, suggesting its excellent OER stability. While $CoP_2$/CC exhibits complete loss of current density within 6h (Supplementary Fig. 26). These observations stand for the important role of V on improving OER stability of $CoP_2$/CC in acidic solution.

To probe the activity and stability origin of V-$CoP_2$/CC for OER in acidic media, a series of post OER characterizations were performed. The $CoP_2$/CC catalyst after OER electrocatalysis was also evaluated for comparison. TEM image (Fig. 5a) of $CoP_2$/CC after OER electrocatalysis shows a very thin Co-oxide layer with the average thickness of ~5 nm around the surface of $CoP_2$. Such a thin Co-oxide layer could not effectively resist the strong oxidation in acidic media, resulting in the worse

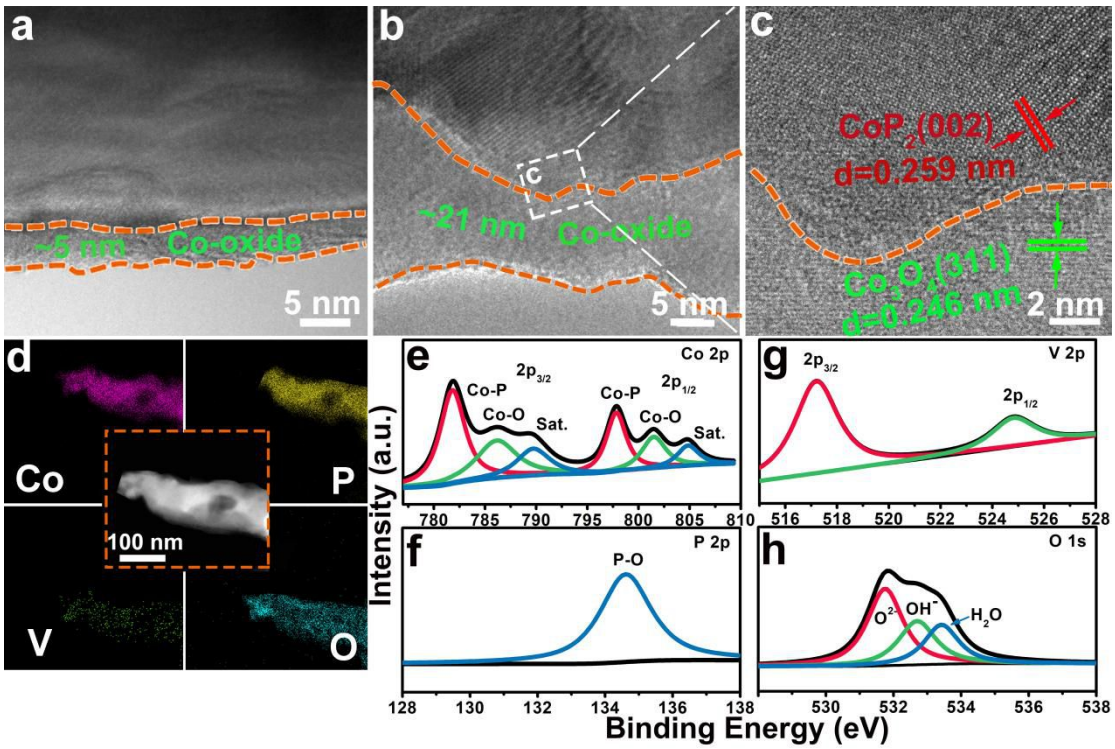


**Fig. 5 Morphology and properties of the post OER.** TEM images of (a) $CoP_2$/CC and (b) V-$CoP_2$/CC. (c) HRTEM image of V-$CoP_2$/CC. (d) STEM image and the corresponding EDX elemental mapping of Co, P, V and O of V-$CoP_2$. XPS spectra of (e) Co 2p, (f) P 2p, (g) V 2p and (h) O 1s in V-$CoP_2$.

stability of $CoP_2$/CC. By contrast, a thicker Co-oxide layer with the average thickness of ~21 nm is observed in the V-$CoP_2$/CC (Fig. 5b). The above results indicate that V incorporation promotes the surface reconstruction of $CoP_2$. HRTEM image of V-$CoP_2$ /CC after OER electrocatalysis further corroborates the existence of inner $CoP_2$ and outer $Co_3O_4$ phases with well crystallization (Fig. 5c). The well-crystallized $Co_3O_4$ layer, which acts as an "armor", can enhance corrosion resistance in acidic OER process. Besides, STEM image and EDX elemental mappings prove the homogeneous distribution of O element in the V-$CoP_2$/CC after OER, in addition to Co, P and V elements (Fig. 5d), confirming the formation of $Co_3O_4$ layer on the $CoP_2$ surface. The dramatic surface chemical change during OER is further reflected by XPS spectra. As shown in Co XPS spectrum, the relative intensities of peaks attributed to Co oxides increase obviously after OER (Fig. 5e). Meanwhile, with respect to P XPS spectrum, the peaks related to Co-P bonds disappear, accompanied by the strengthened peak intensity assigned to P-O bond (Fig. 5f). These results validate the fact of entirely surface oxidation of $CoP_2$ after OER. In the case of V, the binding energies of V $2p_{3/2}$

and V $2p_{1/2}$ peaks related to $V^{4+}$ show positive shift (517.2 and 524.5 eV) (Fig. 5g), indicating the valence of V ionic becomes higher after OER. Besides, O XPS spectrum displays an obvious increased intensity of peak belonging to the adsorbed $H_2O$ (Fig. 5h), suggesting the $H_2O$ adsorption ability is improved by V incorporation. Thus, we deduce the reason that V promotes the surface reconstruction of $CoP_2$ as follows. $V^{4+}$ ion is extremely oxyphilic or hydrophilic because of its highly positive-charged and unfilled d-orbital[47], so that it facilitates the adsorption and dissociation of $H_2O$ to produce more hydroxyl groups. Then, the hydroxyl groups preferentially attach to the unoccupied Co site on the surface (lesser energy barrier)[48], thus leading to the formation of a thicker $Co_3O_4$ layer. In short, $V^{4+}$ promotes the surface reconstruction of $CoP_2$ and the *in-situ* generated thicker $Co_3O_4$ layer can resist corrosion in acidic OER process. What's more, the inner phosphide provides a good conductive platform. The above two points render V-$CoP_2$/CC outstanding activity and stability towards OER.

**Study on catalytic mechanism.** Density functional theory (DFT) calculations were performed to elucidate the origin of the enhanced HER and OER activities. The correlative theoretical models were established (Supplementary Fig. 27). Fig. 6a shows the orbital wave function mappings of $CoP_2$ and V-$CoP_2$. The introduction of V into $CoP_2$ decreases atomic orbital wave function overlap integrals. The change of orbital wave function shrinks energy difference between the highest and lowest orbital levels in the local band and further narrows the local energy bandwidth[49]. As the bandwidth narrows, the d-band center ($E_d$) of $CoP_2$ will shift to keep the number of fixed valence electrons. This can be corroborated by the density of states (DOS). For HER, after V incorporation, the Ed of $CoP_2$ without and with H adsorption relative to Fermi level shift from -1.33 to-1.29 eV and -3.56 to-3.50 eV, respectively (Fig. 6b). The result clearly demonstrates the upshift of d-band center after V incorporation. Besides, the antibonding level is raised and the interaction between the adsorbate and surface is enhanced based on d-band center model[33]. Above results give the intrinsic explication that the upshift of d-band center and the less electrons filled in antibonding states after incorporating V increases the adsorption of hydrogen.

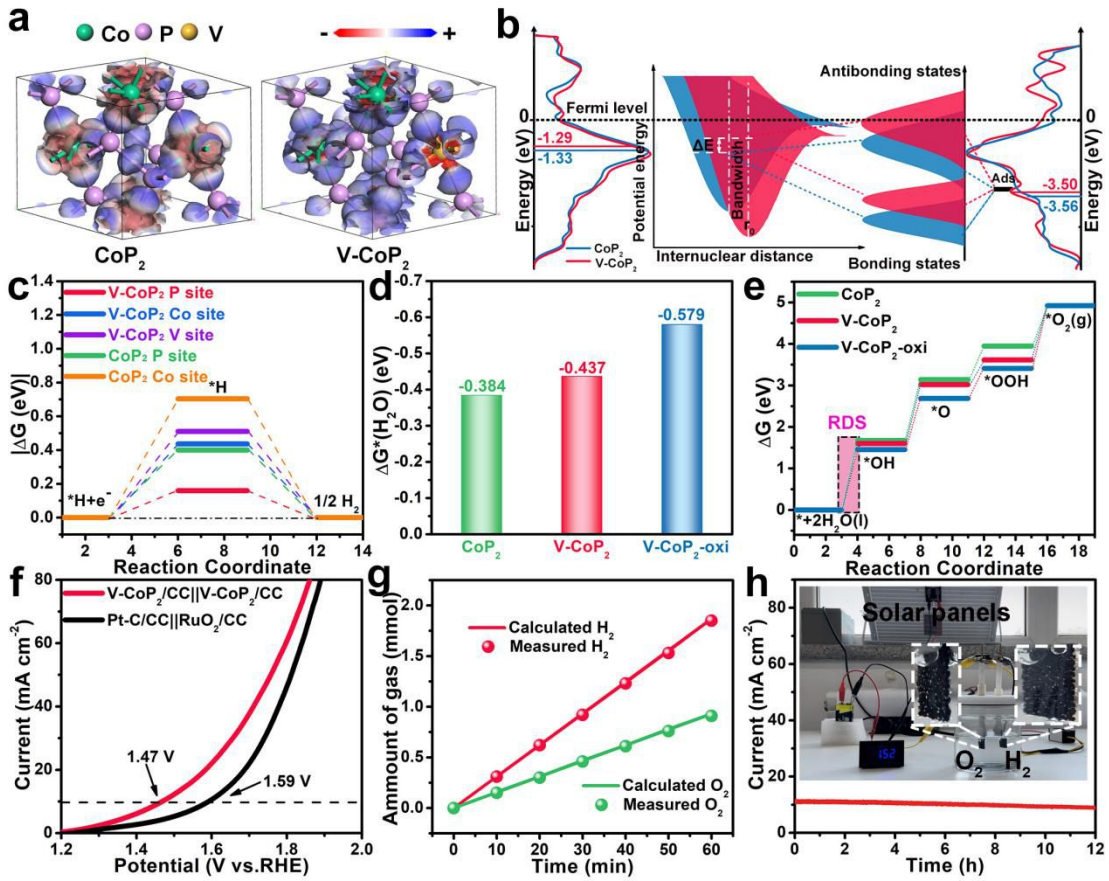


**Fig. 6 DFT calculations and overall water splitting performance.** (a) Orbital wave function mappings of $CoP_2$ and V-$CoP_2$. (b) DOS of $CoP_2$ and V-$CoP_2$ with/without hydrogen adsorption and the schematic diagram of the relation between the narrowed bandwidth and H adsorption strength. (c) Free energy diagram of $CoP_2$ and V-$CoP_2$ with various sites for HER. (d) Calculated $H_2O$ adsorption energy and (e) free energy diagram of $CoP_2$, V-$CoP_2$ and V-$CoP_2$-oxi for OER. (f) LSV curves of two-electrode OWS devices with V-$CoP_2$/CC||V-$CoP_2$/CC and Pt-C/CC||$RuO_2$/CC catalysts. (g) Amount of gas collected and calculated for V-$CoP_2$/CC||V-$CoP_2$/CC. (h) I-t chronoamperometric curve performed at a constant voltage of 1.47 V for 12h. Insert: Demonstration of a water splitting device driven by a solar cell with a voltage of 1.52 V.

Besides, the effects of V on the free energy of hydrogen ($\Delta G_{H^*}$) were investigated. A catalyst with $\Delta G_{H^*}$ closer to zero is regarded as an ideal candidate for HER. V-$CoP_2$ holds a much smaller $|\Delta G_{H^*}|$ than $CoP_2$ (Fig. 6c and Supplementary Fig. 28, Table 5), indicating that V-$CoP_2$ is highly active for HER. Moreover, the smallest $|\Delta G_{H^*}|$ at P site in V-$CoP_2$ indicates that P site is the active site for HER. This can be ascribed to the high electron density at P site induced by V incorporation, as verified by XPS analysis, which is conducive to adsorbing more hydrogen protons.

With respect to OER in acidic media, the water adsorption and the adsorption/desorption of various intermediates (OH*, O* and OOH*) are the key

descriptors. The water adsorbed energy ($E_{H2O}$) on $CoP_2$, V-$CoP_2$ and O-substituted V-$CoP_2$ (V-$CoP_2$-oxi) were calculated, respectively (Supplementary Fig. 29-Fig. 31). The larger $E_{H2O}$ of V-$CoP_2$ (-0.437 eV) than that of $CoP_2$ (-0.384 eV) indicates that V incorporation increases the effective water adsorption (Fig. 6d and Supplementary Table 5), which is in good agreement with XPS observation after OER. Notably, the $E_{H2O}$ further increases to -0.579 eV for V-$CoP_2$-oxi, illustrating that $H_2O$ can be more easily adsorbed and activated on V-$CoP_2$-oxi to promote the OER process[50]. In addition, Fig. 6e shows the free energies of various intermediates adsorbed on $CoP_2$, V-$CoP_2$ and V-$CoP_2$-oxi. The adsorbed energy difference between $\Delta G_{H2O}$ and $\Delta G_{OH*}$ determines the rate-determining step (RDS), which is a vital criterion for evaluating the catalytic activity. V-$CoP_2$-oxi owns the smallest RDS energy difference (1.46 eV), as compared with $CoP_2$ (1.68 eV) and V-$CoP_2$ (1.60 eV), indicating the significant role of oxide species in the catalyst on accelerating OER. Together, above results suggest that V incorporation promotes surface reconstruction to generate a thicker layer of oxides, which favors the OER kinetics and optimizes the adsorption energies of water and oxygen species, thereby improving OER activity and stability.

**Overall water splitting performance.** In light of the outstanding bifunctional catalytic feature of V-$CoP_2$/CC for acidic HER and OER, two identical V-$CoP_2$/CC electrodes were employed to assemble two-electrode overall water splitting (OWS) device. V-$CoP_2$/CC||V-$CoP_2$/CC merely requires a low voltage of 1.47 V to achieve the current density of 10 mA $cm^{-2}$, which outperforms the Pt-C/CC||$RuO_2$/CC-based electrolyzer (1.59 V@10 mA $cm^{-2}$) (Fig. 6f). Remarkably, the overall water splitting performance is also superior to most of the reported noble metal-based electrocatalysts in acidic media (Supplementary Table 6). Additionally, V-$CoP_2$/CC||V-$CoP_2$/CC shows high Faradaic efficiencies close to 100% for both HER and OER (Fig. 6g), demonstrating the high reaction efficiency and negligible side reactions. V-$CoP_2$/CC//V-$CoP_2$/CC also exhibits superb stability with no obvious decrease in activity after continuous operation at 1.47 V for 12h (Fig. 6h). Impressively, the electrolyzer can be driven by a solar cell with a low voltage of 1.52

V, in which many gas bubbles can be observed, indicating its potential for coupling with renewable energy sources (inset of Fig. 6h and Supplementary Movie 1).

In summary, we have designed V-incorporated $CoP_2$ porous nanowires anchored on carbon cloth (V-$CoP_2$/CC) as a bifunctional electrocatalyst for overall water splitting in acidic media. The lattice expansion of $CoP_2$ caused by V incorporation decreases the atomic wave function overlap and renders the upshift of d-band center, as verified by a series of structural characterizations and theoretical analysis. The upshift of d-band center in V-$CoP_2$ induces more hydrogen adsorption on P sites, which gives rise to an enhanced HER activity. In addition, a thicker $Co_3O_4$ layer on the $CoP_2$ surface that is generated from surface reconstruction promoted by V incorporation, improves acid-corrosion resistance and optimizes the adsorption free energies of water and oxygen species, accounting for the catalytic OER performance. The catalyst exerts superb catalytic performances for both HER and OER. Impressively, the electrolyzer requires a low voltage of 1.47 V at 10 mA $cm^{-2}$, and can be easily driven by a solar cell. This work offers a new approach to design efficient electrocatalysts through lattice engineering induced by heteroatom incorporation.

## Methods

**Chemicals.** Cobalt nitrate hexahydrate ($Co(NO_3)_2 \cdot 6H_2O$), ammonium metavanadate ($NH_4VO_3$), ammonium fluoride ($NH_4F$, analytical reagent 98%) and urea ($CO(NH_2)_2$) were purchased from Aladdin Reagent Co., Ltd. Sodium hypophosphite ($NaH_2PO_2$, analytical reagent 99.5%) was purchased from Kermel. Ethanol was obtained from Tianjin Kermel Chemical Reagent Co., Ltd. All chemicals were used as received without any further purification.

**Synthesis of V-$CoP_2$ porous nanowire.** In a typical synthesis, 0.05 mmol of $NH_4VO_3$, 0.95 mmol of $Co(NO_3)_2 \cdot 6H_2O$, 5 mmol of $CO(NH_2)_2$, and 2 mmol of $NH_4F$ were dissolved in 25 mL of deionized water and stirred for 2h to form a homogeneous solution. Afterward, the mixture was transferred to a 50-mL Teflon-lined stainless steel autoclave containing CC (3 × 3 $cm^{-2}$) and hydrothermally treated at 120 $^oC$ for 4h. After cooling to the room temperature, the V-CoOOH precursors grown on the CC (V-CoOOH/CC) were ultrasonically cleaned with deionized water and ethanol for several times and dried in an oven at 60 $^oC$ overnight. Finally, 1.2 g of $NaH_2PO_2$ powder and V-CoOOH/CC were placed on the upstream and downstream of the quartz tube,

respectively. Before phosphorization, $N_2$ was purged for 20 min to remove the air. The V-CoOOH/CC was heated at 600 $^oC$ with a ramp rate of 2 $^oC$ $min^{-1}$ and maintained at 600 $^oC$ for 2h. After cooling to room temperature, the V-$CoP_2$/CC was harvested, in which the V incorporation ratio is 5%. For comparison, $CoP_2$/CC were prepared with similar process to that employed for the fabrication of V-$CoP_2$/CC, except that only adding Co source. Additionally, a series of control experiments were performed. Specifically, the corresponding phosphorization products with other hydrothermal times of 2 and 6h were prepared (labeled as V-$CoP_2$/CC-2 and V-$CoP_2$/CC-6). The V-$CoP_2$/CC samples with other V incorporation ratios of 2.5% and 10% were prepared (named as V-$CoP_2$/CC-2.5% and V-$CoP_2$/CC-10%). The V-CoOOH/CC was treated at the phosphorization temperatures of 500 and 700 °C and labeled as V-$CoP_2$/CC-T500 and V-$CoP_2$/CC-T700. The V-CoOOH/CC was phosphatized for 1 and 3h and tagged as V-$CoP_2$/CC-T1h and V-$CoP_2$/CC-T3h.

**Material Characterizations.** The crystal phase of the samples were determined by Bruker D8 diffractometer X-ray powder diffraction (XRD) with Cu Kα radiation and the acceleration voltage of 40 kV). Scanning electron microscopy (SEM: Hitachi s-4800) and transmission electron microscopy (TEM: JEM-2100) with an acceleration voltage of 200 kV and energy dispersive X-ray spectroscopy (EDX) were used to analyze the morphology of samples. Raman was conducted with a Jobin Yvon HR 800 micro-Raman spectrometer at 457.9 nm. X-ray photoelectron spectroscopy (XPS) characterization was conducted on a VG ESCALAB MK II with the excitation source of Mg Kα (1253.6 eV) achromatic X-ray radiation. The $N_2$ adsorption-desorption isotherms of the samples were performed by Micromeritics Tristar II. Scanning Kelvin Probe ((SKP5050 system, Scotland) were performed in ambient atmosphere with a gold electrode as the reference electrode. The amount of gases was quantified by gas chromatography (Aglient, 7820A).

**Electrochemical measurements.** Electrochemical measurements were performed with a CHI660E electrochemical workstation. A three-electrode configuration at room temperature was used, where self-supported electrocatalytic materials, graphite rod and saturated calomel electrode (SCE) were used as the work electrode, the auxiliary electrode and the reference electrode, respectively. All the potentials were recorded with respect to the reversible hydrogen electrode (RHE) and 95% iR-corrected according to the equation $E_{RHE}= E_{SCE} + 0.244\ V+0.059pH-iR$.

Linear sweep voltammetry was collected in 0.5 M $H_2SO_4$ with the scan rate of 5 mV $s^{-1}$. The potential cycling stability test was examined by taking continuous cyclic voltemmgrams (CVs) at a scan rate of 100 mV $s^{-1}$. The I-t chronoamperometric test was tested for 12h at the potential required 10 mA $cm^{-2}$. Electrochemical impedance spectroscopy (EIS) was performed with frequency range from 1 Hz to 100 kHz. CV curves were conducted with different rates from 20 to 100 mV $s^{-1}$ to determine double-layer capacitance. The voltage range for overall water splitting was tested from 1 to 2 V. The Faradaic efficiencies for HER and OER were measured by comparing the experimental and theoretical amounts of $H_2$ and $O_2$. In the test, potentiostatic electrolysis was employed at 100 mA $cm^{-2}$ for 1h.

**Computational details.** The projector augmented-wave (PAW) technique with the set plane-wave energy cutoff of 300 eV was conducted[51]. Perdew-Burke-Ernzerhof (PBE) functional was employed to settle the correlation-exchange energies of the systems[52]. The sampling over Brillouin zone was treated by a (2×2×1) Monkhorst-Pack grid, and a vacuum slab with the length of 10 Å was placed along z axis on each slab to avoid the pseudo interactions between periodic images. Geometry optimization was repeated until the total energy tolerance was converged to $2*10^{-5}$ eV and the changes of the force on the atoms less than 0.03 eV/Å.

## References


1. Seh Z. W. et al. Combining theory and experiment in electrocatalysis: insights into materials design. *Science* **355**, 146 (2017).
2. Dinh C. T. et al. Multi-site electrocatalysts for hydrogen evolution in neutral media by destabilization of water molecules. *Nat. Energy* **4**, 107114 (2019).
3. Chen L., Dong X., Wang Y. & Xia Y. Separating hydrogen and oxygen evolution in alkaline water electrolysis using nickel hydroxide. *Nat. Commun.***7**, 11741 (2016).
4. Fan X. et al. Defect-enriched iron fluoride-oxide nanoporous thin films bifunctional catalyst for water splitting. *Nat. Commun.* **9**, 1809 (2018).
5. Yan H. et al. Holey reduced graphene oxide coupled with an $Mo_2N$-$Mo_2C$ heterojunction for efficient hydrogen evolution. *Adv. Mater.* **30**, 1704156 (2018).
6. Liu J. et al. Ultrathin amorphous cobalt-vanadium hydr(oxy)oxide catalysts for the oxygen evolution reaction. *Energy Environ. Sci.* **11**, 1736-1741 (2018).
7. Hao S. et al. Dopants fixation of ruthenium for boosting acidic oxygen evolution stability and activity. *Nat. Commun.* **11**, 5368 (2020).
8. Schalenbach M. A perspective on low-temperature water electrolysis-challenges in alkaline and acidic technology. *Int. J. Electrochem. Sci. **13**,* 1173-1226 (2018).

9. An L. et al. Recent development of oxygen evolution electrocatalysts in acidic environment. *Adv. Mater.* **33**, 2006328 (2021).
10. Zhu J. et al. Regulative electronic states around ruthenium/ruthenium disulphide heterointerfaces for efficient water splitting in acidic media. *Angew. Chem. Int. Ed.* **133**, 1-8 (2021).
11. Reier T., Nong H. N., Teschner D., Schlögl R. & Strasser P. Electrocatalytic oxygen evolution reaction in acidic environments-reaction mechanisms and catalysts. *Adv. Energy Mater.* **7**, 1601275 (2017).
12. Li L. et al. Recent progress in advanced electrocatalyst design for acidic oxygen evolution reaction. *Adv. Mater.* **33**, 2004243 (2021).
13. Zhang H., Maijenburg A. W., Li X., Schweizer S. L. & Wehrspohn R. B. Bifunctional heterostructured transition metal phosphides for efficient electrochemical water splitting. *Adv. Funct. Mater.* **30**, 2003261 (2020).
14. Zou X. & Zhang Y. Noble metal-free hydrogen evolution catalysts for water splitting. *Chem. Soc. Rev.* **44**, 5148-5180 (2015).
15. Fu H. et al. Two dimensional porous molybdenum phosphide/nitride heterojunction nanosheets for pH-universal hydrogen evolution reaction. *Angew. Chem. Int. Ed.* **60**, 6673-6681 (2020).
16. Zhou W. et al. Recent developments of carbon-based electrocatalysts for hydrogen evolution reaction. *Nano Energy* **28**, 29-43 (2016).
17. Han N. et al. Nitrogen-doped tungsten carbide nanoarray as an efficient bifunctional electrocatalyst for water splitting in acid. *Nat. Commun.* **9**, 924 (2018).
18. Wu D. et al. Efficient overall water splitting in acid with anisotropic metal nanosheets. *Nat. Commun.* **12**, 1145 (2021).
19. Li H. et al. Phosphorus-rich colloidal cobalt diphosphide ($CoP_2$) nanocrystals for electrochemical and photoelectrochemical hydrogen evolution. *Adv. Mater.* **31**, 1900813 (2019).
20. Hou C. C., Zou L., Wang Y. & Xu Q. MOF-mediated fabrication of a porous 3D superstructure of carbon nanosheets decorated with ultrafine cobalt phosphide nanoparticles for efficient electrocatalysis and zinc-air batteries. *Angew. Chem. Int. Ed.* **59**, 21360-21366 (2020).
21. Zai S. F., Zhou Y. T., Yang C. C. & Jiang Q. Al, Fe-codoped CoP nanoparticles anchored on reduced graphene oxide as bifunctional catalysts to enhance overall water splitting. *Chem. Eng. J.* **421**, 127856 (2021).
22. Wei Y. et al. Metal-organic framework derived NiCoP hollow polyhedrons electrocatalyst for pH-universal hydrogen evolution reaction. *Chin. Chem. Lett.* **32**, 119-124 (2021).
23. Shi Y. & Zhang B. Recent advances in transition metal phosphide nanomaterials: synthesis and applications in hydrogen evolution reaction. *Chem. Soc. Rev.* **45**, 1529-1541 (2016).
24. Wu Z., Huang L., Liu H. & Wang H. Element-specific restructuring of anion- and cation-substituted cobalt phosphide nanoparticles under electrochemical water-splitting conditions. *ACS Catal.* **9**, 2956-2961 (2019).

25. Chang J. et al. Surface oxidized cobalt-phosphide nanorods as an advanced oxygen evolution catalyst in alkaline solution. *ACS Catal.* **5**, 6874-6878 (2015).
26. Zhu Y., Zhang T., An T., Zong Y. & Lee J. Y. Unraveling the electrocatalytically active sites and stability of Co & Co oxides on nanocarbon for oxygen evolution reaction in acid solution. *J. Energy Chem.* **49**, 8-13 (2020).
27. Xu K. et al. Controllable surface reorganization engineering on cobalt phosphide nanowire arrays for efficient alkaline hydrogen evolution reaction. *Adv. Mater.* **30**, 1703322 (2018).
28. Kou Z. et al. Potential-dependent phase transition and Mo-enriched surface reconstruction of γ-CoOOH in a heterostructured Co-$Mo_2C$ precatalyst enable water oxidation. *ACS Catal.* **10**, 4411-4419 (2020).
29. Li Y. et al. Processable surface modification of nickel-heteroatom (N, S) bridge sites for promoted alkaline hydrogen evolution. *Angew. Chem. Int. Ed.* **58**, 461-466 (2019).
30. Sun Y. et al. Nitrogen-doped cobalt diselenide with cubic phase maintained for enhanced alkaline hydrogen evolution. *Angew. Chem. Int. Ed.* **60**, 2-10 (2021).
31. Wang X., Meng L., Li B. & Gong Y. Heteroatoms/molecules to tune the properties of 2D materials. *Mater. Today* **47**, 108-130 (2021).
32. Böhm D. et al. V(III)-doped nickel oxide-based nanocatalysts for electrochemical water splitting: influence of phase, composition, and doping on the electrocatalytic activity. *Chem. Mater.* **32**, 10394-10406 (2020).
33. Chen Z. et al. Tailoring the d-band centers enables $Co_4N$ nanosheets to be highly active for hydrogen evolution catalysis. *Angew. Chem. Int. Ed.* **57**, 5076-5080 (2018).
34. Li Z. et al. V "bridged" Co-O to eliminate charge transfer barriers and drive lattice oxygen oxidation during water-splitting. *Adv. Funct. Mater.* **31**, 2008822 (2020).
35. Tao X., Matthews A. & Leyland A. On the nitrogen-induced lattice expansion of a non-stainless austenitic steel, Invar 36®, under triode plasma nitriding. *Metall. Mater. Trans. A* **51**, 436-447 (2019).
36. Liu G. et al. Hydrogen-intercalation-induced lattice expansion of Pd@Pt core-shell nanoparticles for highly efficient electrocatalytic alcohol oxidation. *J. Am. Chem. Soc.* **143**, 11262-11270 (2021).
37. Chen J. et al. Catalytic activity atlas of ternary Co-Fe-V metal oxides for the oxygen evolution reaction. *J. Mater. Chem. A* **8**, 15951-15961 (2020).
38. Dong X. et al. One-dimensional $CO_9S_8$-$V_3S_4$ heterojunctions as bifunctional electrocatalysts for highly efficient overall water splitting. *Sci. China Mater.* **64**, 1396-1407 (2021).
39. Chen C. et al. Trapping $[PMo_{12}O_{40}]^{3-}$ clusters into pre-synthesized ZIF-67 toward MoxCoxC particles confined in uniform carbon polyhedrons for efficient overall water splitting. *Chem. Sci.* **9**, 4746-4755 (2018).

40. Yang G. et al. Interfacial engineering of $MoO_2$-FeP heterojunction for highly eefficient hydrogen evolution coupled with biomass electrooxidation. *Adv. Mater.* **32**, 2000455 (2020).
41. Dong X. et al. 3D hierarchical V-Ni-based nitride heterostructure as a highly efficient pH-universal electrocatalyst for the hydrogen evolution reaction. *J. Mater. Chem. A* **7**, 15823-15830 (2019).
42. Fan K. et al. Hollow iron-vanadium composite spheres: a highly efficient iron-based water oxidation electrocatalyst without the need for nickel or cobalt. *Angew. Chem. Int. Ed.* **56**, 3289-3293 (2017).
43. Cai Z. et al. Hierarchical whisker-on-sheet NiCoP with adjustable surface structure for efficient hydrogen evolution reaction. *Nanoscale* **10**, 7619-7629 (2018).
44. Deng L. et al. Rational design of schottky heterojunction with modulating surface electron density for high-performance overall water splitting. *Appl. Catal. B* **299**, 120660 (2021).
45. Jeung Y. et al. 2D-structured V-doped Ni(Co,Fe) phosphides with enhanced charge transfer and reactive sites for highly efficient overall water splitting electrocatalysts. *J. Mater. Chem. A* **9**, 12203-12213 (2021).
46. Yan H. et al. Synergism of molybdenum nitride and palladium for high-efficiency formic acid electrooxidation. *J. Mater. Chem. A* **6**, 7623-7630 (2018).
47. Cui Z. et al. Synthesis of structurally ordered $Pt_3Ti$ and $Pt_3V$ nanoparticles as methanol oxidation catalysts. *J. Am. Chem. Soc.* **136**, 10206-10209 (2014).
48. Subbaraman R. et al. Enhancing hydrogen evolution activity in water splitting by tailoring $Li^+$-$Ni(OH)_2$-Pt interfaces. *Science* **334**, 1256-1260 (2011).
49. Cai J. et al. N-induced lattice contraction generally boosts the hydrogen evolution catalysis of P-rich metal phosphides. *Sci. Adv.* **6**, eaaw8113 (2020).
50. Yan H. et al. Anion-modulated HER and OER sctivities of 3D Ni-V-based interstitial compound heterojunctions for high-efficiency and stable overall water splitting. *Adv. Mater.* **31**, 1901174 (2019).
51. Blochl P. E. Projector augmented-wave method. *Phys. Rev. B* **50**, 17953-17979 (1994).
52. Perdew J. P., Burke K. & Ernzerhof M. Generalized gradient approximation made simple. *Phys. Rev. Lett.* **77**, 3865-3868 (1996).

**Acknowledgements**

This research was supported by the National Key R&D Program of China (2018YFB1502401), the National Natural Science Foundation of China (21631004, U20A20250, 22171074, 21805073, 91961111, 21901064), the Natural Science Foundation of Heilongjiang Province (YQ2021B009).

**Author contributions**

H. G. F. and H. J. Y. conceived the idea. H. J. Y. and Y. W. designed the experiments, collected and analyzed the data. Y. Q. J., A. P. W., G. C. Y. and Y, L. assisted with the experiments and characterizations. H. G. F., H. J. Y. and Y. W. co-wrote the manuscript. All authors discussed the results and commented on the manuscript.

**Additional information**

**Supplementary Information** accompanies this paper at http://www.nature.com/naturecommunications

**Competing financial interests**: The authors declare no competing financial interests.

**Reprints and permission** information is available online at http://npg.nature.com/reprintsandpermissions/

## Supplementary Files

This is a list of supplementary files associated with this preprint. Click to download.

- SupplementaryMovie1.mp4
- Supportinginformation.pdf